Engineering Structures 311 (2024) 118164

Contents lists available at ScienceDirect

Engineering Structures

journal homepage: www.elsevier.com/locate/engstruct

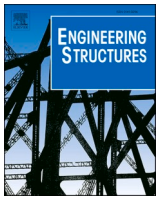

Long-term deformation monitoring of a steel-truss arch bridge using PSI technique refined by temperature field analysis

Yun Zhou [a,b], Guanwang Hao [b,*], Jianwei Chen [b], Junjie Wei [b], Jiayuan Zheng [b]

[a] Key Laboratory for Damage Diagnosis of Engineering Structures of Hunan Province, Hunan University, Changsha 410082, China
[b] College of Civil Engineering, Hunan University, Changsha 410082, China

ARTICLE INFO

Keywords:
Steel-truss arch bridge
Structural health monitoring
Persistent scatterer interferometry
Meteorological shared data
Temperature field
Bridge deformation

ABSTRACT

Satellite-based Interferometric Synthetic Aperture Radar (InSAR) is a radar technique that can identify millimeter-level deformation of long-span bridges. However, the technique focuses on the influence of air temperature on long-span bridge deformation, neglecting the difference between the structural temperature field and the ambient temperatures. This oversight leads to a diminished precision in the estimation of the thermal dilation phase of the InSAR technique. To address this limitation, this study presents a long-term deformation monitoring methodology for long-span bridges by integrating Persistent Scatterer Interferometry (PSI) with a structure's temperature field. A finite-element (FE) model is constructed for investigating the key structural members of a bridge, and, utilizing ambient air temperature sourced from a meteorological data sharing platform, a transient heat transfer analysis is conducted to obtain the time-dependent temperature distribution. The temperature field at the moment of SAR imaging is utilized by the PSI technique, instead of the ambient air temperature. The proposed method was applied to monitor the deformation of a long-span steel truss arch bridge using 163 Sentinel-1A acquisitions and 35 COSMO-SkyMed acquisitions, to obtain the line of sight displacement. The displacements derived from different data sources were analyzed and subsequently compared with FE calculation results and on-site measurement data. The observed relative error of thermal dilation velocity using the PSI technology refined by bridge temperature field (RPSI) spanned from − 4.52 % to 4.50 %, indicating the estimations of thermal dilation were well refined. Results demonstrate that RPS succeeds in large-span bridges deformations measurement, providing a valuable tool for realizing lightweight monitoring of bridge structures.

1. Introduction

Bridge deformation, which reflects the overall stiffness of the bridge structure, is crucial for structural performance assessment [1,2]. Bridge displacement measurement techniques can be categorized into contact and non-contact measurement methods. Contact measurement methods such as using displacement meters, inclinometers, connecting tubes, global navigation satellite systems, and fully automated total stations, are widely used due to their reliability. However, they are limited by the local observation and the high costs, especially for continuous monitoring tasks. While the non-contact measurement methods, including machine vision technique, microwave radar sensing technique, photogrammetric technique, and 3D laser scanning technique, have notably improved the efficiency of bridge displacement measurement, the accuracy of these non-contact methods may be compromised by environmental conditions and the distances involved in testing. Space-to-Earth observation techniques, represented by the Interferometric Synthetic Aperture Radar (InSAR) technique, extracts the target deformation through slant range phase interferometry, which can obtain large-area surface deformation at all-times and under all weather conditions. The InSAR technique which has been extensively used in infrastructure deformation monitoring, including buildings [3], highways [4], railways [5], dams and embankments [6], also presents a much more cost-effective solution for deformation monitoring.

Abbreviations: InSAR,, Interferometric Synthetic Aperture Radar; CSK,, COSMO-SkyMed; S1A,, Sentinel-1A; PS,, Persistent scatterer; RPSI,, Refined PSI technique; PSI,, Persistent Scatterer Interferometry; FE, Finite-element; MAE, Mean absolute error; RMSE, Root mean squared error; MaxAE, Maximum absolute error; S1A-PSI, S1A data processed with the PSI technique; CSK-PSI, CSK data processed with the PSI technique; S1A-RPSI, S1A data processed with the RPSI technique; CSK-RPSI, CSK data processed with the RPSI technique; TDV, Thermal dilation velocity.

* Corresponding author.
E-mail address: gwh0114@hnu.edu.cn (G. Hao).

https://doi.org/10.1016/j.engstruct.2024.118164
Received 14 November 2023; Received in revised form 11 March 2024; Accepted 4 May 2024

Relying on the assistance of medium to high-resolution SAR satellites, the accuracy of deformation measurements via InSAR technique has been effectively enhanced. However, the practical application of InSAR has been restricted by influence factors such as atmospheric delays, temporal decorrelation, and spatial decorrelation. The Persistent Scatterer Interferometry (PSI) approach, which focuses on reliable and stable points in a series of SAR images, addresses these limitations and is applied for small movements monitoring. Huang et al. [7] utilized PSI technique to monitor displacements in a high-speed railway bridge, and the PSI-measured displacements was compared with in-situ measurements results. Ma et al. [8] conducted a tentative test for measuring the sub-millimeter settlement and uplift of a bridge, in which the persistent scatterer (PS) and distributed scatterer were jointly detected to increase point density. Qin et al. [9] proposed a method to integrate the Point-like Targets selection strategies of PS and small baseline interferometric processing, which effectively boosted the robustness of the deformation estimation for cable-stayed bridges. Caspani et al. [10] extracted the displacement of a highway bridge using the PSI technique and investigated its correlation with environmental phenomena, specifically variations in air temperature and river water flow. Moreover, the structural movement velocity acquired using PSI-derived displacement time series can serve as an indicator for bridge safety assessment. Based on both ascending and descending SAR acquisitions, a two-dimensional displacement configuration of multi-span bridges with properly defined error bounds was determined, demonstrating the effectiveness of the InSAR technique in early damage detection [11]. Sousa [12] processed 52 S1A images from 1995 to 2001 using the PSI technique, successfully tracing back to the historical subsidence information of a bridge, revealing that the maximum deformation rate before the bridge collapse reached 20 mm/year. A displacement map for the structure was generated by Milillo et al. [13] based on the InSAR technique and Markov Chain Monte Carlo approach, which indicated that the bridge was undergoing an increased magnitude of deformations over time prior to its collapse. Using the SqueeSAR algorithm, the time series of bridge deformations with millimeter-range precision were obtained, indicating that no permanent deformations occurred in the post-tensioned segments during the 1.3-year monitoring period [14]. Displacement data obtained by InSAR was combined with structural and collapse analysis by Farneti et al., thereby enabling the recognition of potentially critical conditions and the prediction of failure times for bridges experiencing slow landslide-induced movements [15]. The feasibility of the PSI technique in monitoring the long-term deformation of bridges has been effectively validated in previous studies. Thermal dilation significantly contributes to the deformation of long-span bridges, making it crucial to the precision of PSI measurements [16,17]. The InSAR technique was used to detect the millimeter-level motion on ground structures and the thermal sensitivity was introduced by Cusson et al. [18] to monitor bridge behavior. A linear regression model between InSAR longitudinal displacement and ambient air temperature was developed by Huang et al. [7] showing that the PSI-measured displacements were in good agreement with the in-situ measurements. Lazecky et al. [19] utilized an approach to identify the thermal expansion component, using an additional parameter to search for a relationship between interferogram phase values and temperature differences at the times of image acquisition. Qin. et al. [20,21] introduced the linear thermal dilation estimation into the traditional differential InSAR method, which significantly improved the thermal dilation separation for arch bridges.

In previous research on the estimation of thermal dilation using the PSI technique, which the air temperature was utilized, the difference between the bridge's temperature field and the ambient air temperature was generally ignored. The temperature field of a long-span bridge is variable and complicated, influenced by periodically time-varying solar radiation and continuous structural heat exchange with the surrounding environment [22–24]. Based on meteorological data measured by on-site installed sensors, computational methodologies for bridge temperature fields can be established [25]. Lu et al. [26] studied the concrete bridge box girder temperature distribution and thermal effect under solar radiation and the thermal load. A two-dimensional FE model for a typical section of a box girder of a long-span suspension and cable-stayed bridge was constructed, with which the time-dependent temperature distribution was determined based on ambient temperature measurements through transient heat transfer analysis [27–29]. Based on long-term temperature monitoring data and statistical analysis, Xia et al. [30] developed a time-varying solar radiation model that incorporates the impact of real-time weather fluctuations, including variations in cloud cover. A vertical discrete and dimensionality-reduced model for rapid temperature loads calculation of bridge structures were proposed by Fan et al. [31] The random forest model was used to predict the sectional effective temperature, taking into consideration the environmental and meteorological factors (temperature, solar radiation, humidity, wind speed, and direction) [32]. Xia et al. [33] developed a unified approach of heat-transfer and structural analyses to calculate the temperature distribution and the associated responses of an entire structure by integrating the field monitoring data. A refined 3D model of a three-tower cable-stayed bridge, of which the thermal boundary conditions were determined using environmental field monitoring data, was constructed to facilitate a comprehensive global 3D heat-transfer analysis [34]. Abid et al. and Lu et al. [35,36] described the construction and instrumentation of an experimental box-girder segment, aiming to analyze the temperature distributions in concrete bridges under the fluctuation of air temperature and solar radiation thermal loads. Consequently, to analyze the temperature effects on bridges based on the field monitoring data, it is essential to establish the on-site monitoring system to collect extensive temperature measurement data.

To the best of the authors' knowledge, few studies have emphasized the impact of the difference between air temperature and bridge temperature field on the calculation accuracy of thermal dilation of the PSI technique. This study therefore focuses on analyzing the temperature field of bridge structures by utilizing meteorological shared data, with the aim of overcoming the limitations due to insufficient temperature measurement data and of refining the PSI technique (RPSI) through the bridge temperature field for long-term deformation monitoring. Transient thermal analysis was conducted based on equivalent air temperature and equivalent heat transfer coefficient, which were derived from meteorological shared data (temperature, wind speed, and precipitation) obtained from a weather station near the case study bridge. This analysis determined the temperature distribution of the key structural members, thereby providing a time-dependent temperature for estimating the thermal dilation phase of the RPSI technique. Applying this novel approach, S1A (medium-low resolution) and CSK (high resolution) imagery datasets were processed to derive the line of sight (LOS) displacement time series for the case study steel-truss arch bridge. By integrating the SAR imaging LOS geometry with the structural characteristics of the bridge, the bridge's longitudinal displacement time series was derived. The RPSI-based displacements were then compared with PSI-based displacements, FE simulated results and field monitoring data, to verify the reliability and accuracy of the proposed approach. The outcomes of this study can offer technical support for achieving lightweight monitoring of the long-term deformation of long-span bridges, thereby facilitating sensor-free and cost-effective structural health assessments.

2. Methodology

2.1. RPSI technique

Lightweight monitoring involves the use of minimal equipment, materials, and labor for structural health monitoring, highlighting its status as an optimal solution that balances precision with economic viability. The PSI technique is a feasible lightweight monitoring method

owing to its cost-efficiency and accuracy in measurement. PSI technique examines SAR time-series, concentrating on steady, point-like scatterers that exhibit no speckle and generate a definitive signal response [37,38]. Assuming N SAR images covering the observation area over a certain period are available, one image is selected as the master image considering temporal baseline, spatial baseline, and Doppler centroid frequency, with the remaining images serving as slave images. The N-1 slave images are co-registered and resampled to the spatial domain of the master image, resulting in N-1 interferometric pairs. Utilizing digital elevation models, differential interferometric processing is applied to these interferometric pairs, yielding differential phases for each PS point as shown in the following equation:

$$\psi = \varphi_{\text{ref}} + \varphi_{\text{top}} + \varphi_{\text{def}} + \varphi_{\text{atm}} + \varphi_{\text{noi}} \tag{1}$$

where the interferometric phase in SAR images is affected by various error sources, which can be categorized into five components: φ_{ref} represents the orbit estimation errors, φ_{top} is the height errors, φ_{def} means the terrain displacement in LOS path, φ_{atm} indicates the atmospheric phase delay, and φ_{noi} represents the thermal noise and other error components. After differential processing the phase contains the linear deformation phase, elevation phase, and residual phase, as follows:

$$\psi = \frac{4\pi}{\lambda} t \cdot v + \frac{4\pi}{\lambda R \sin\theta} B \cdot \varepsilon + \varphi_{\text{res}} \tag{2}$$

where λ represents the radar wavelength; R is the slant range from the radar to the ground target; θ denotes the radar incidence angle; B stands for the vertical baseline; ε is the elevation error caused by the vertical structural displacement of the bridge; t refers to the temporal baseline; v is the linear deformation rate along the LOS direction, and φ_{res} signifies the residual phase, which includes atmospheric contributions, nonlinear deformation phase, and noise.

The temperature is a primary factor influencing the long-term deformation of long-span bridges. Hence, thermal dilation parameters are introduced to the nonlinear deformation of the interferometric model by the RPSI technique, as expressed by the following equation:

$$\psi = \frac{4\pi}{\lambda} t \cdot v + \frac{4\pi}{\lambda R \sin\theta} B \cdot \varepsilon + \frac{4\pi}{\lambda} T_{\text{tf}} \cdot k + \varphi_{\text{res}} \tag{3}$$

where T_{tf} denotes the temperature field of the bridge structure corresponding to the PS points at each image acquisition, and k is the thermal expansion coefficient.

To accurately estimate the parameters of the interference phase model, this study conducted a quadratic difference interference analysis on the connections between PS points within the Delaunay triangulation network formed by PS points. The expression for the quadratic difference interference model is as follows:

$$\Delta\psi = \frac{4\pi}{\lambda} t \Delta v + \frac{4\pi}{\lambda R \sin\theta} B \Delta\varepsilon + \frac{4\pi}{\lambda} T_{\text{tf}} \Delta k + \Delta\varphi_{res} \tag{4}$$

where $\Delta\psi$ is the differential interferometric wrapped phase, Δv denotes the unknown differential velocity, $\Delta\varepsilon$ stands for the differential elevation error, Δk represents the differential thermal expansion parameter, and $\Delta\varphi_{res}$ refers to the residual phase component.

The estimation of parameters Δv, $\Delta\varepsilon$, and Δk is aimed at searching for the optimal solution of the objective function, meaning finding the parameter estimates that correspond to the maximum coherence coefficient of γ. This function is depicted as follows:

$$\gamma = \frac{1}{N} \sum_{i=1}^{N} \exp\left(j\Delta\psi_{obs}^{i} - \Delta\psi_{m}^{i}(\Delta v, \Delta\varepsilon, \Delta k)\right) \tag{5}$$

where $\Delta\psi_{obs}^{i}$ represents the observed phase difference, $\Delta\psi_{m}^{i}$ denotes the model's calculated value, and N signifies the number of interference pairs.

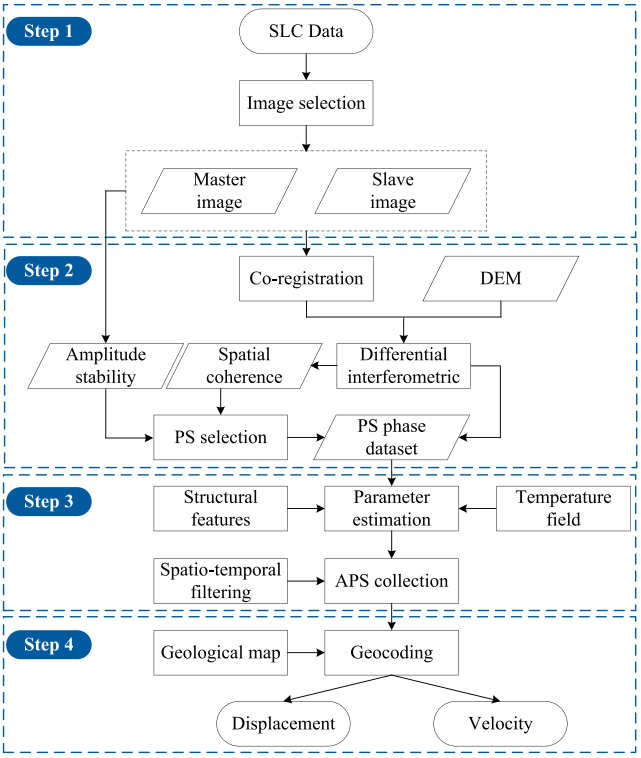

Fig. 1. RPSI processing flow.

The thermal dilation phase after differential processing can be expressed as follows:

$$\Delta\psi_{T}^{i} = \frac{4\pi}{\lambda} \Delta T_{\text{tf}}{}^{i} k \tag{6}$$

where $\Delta T_{\text{tf}}{}^{i}$ is the difference of the bridge temperature between the two acquisitions.

The RPSI technique involves four steps: images co-registration, PS points identification, atmospheric phase screen (APS) estimation and removal, and deformation recovery. The workflow of this technique is depicted in Fig. 1 and involves the following steps:

(1) Images co-registration. The master image is chosen from N SAR images based on the principle of minimal temporal and spatial baselines. The coherence coefficient method is employed to register all slave images with the master image.

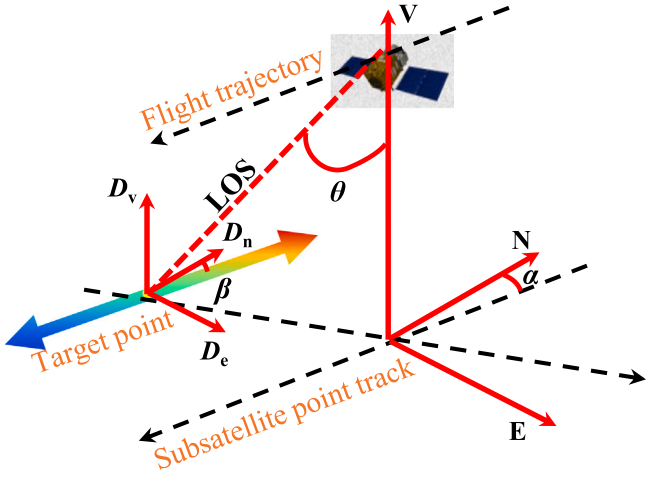

Fig. 2. SAR observation geometry of the target point.

(2) PS points identification. Using precise orbital vectors and interferometric geometric relationships, the reference phase is removed. The topographic phase is eliminated with digital elevation models, producing a differential interferometric series map. The amplitude time series is calculated for each pixel within the image, and the PS points are selected based on the amplitude residual information.

(3) APS estimation and removal. The bridge temperature field is utilized to estimate the thermal dilation component of RPSI technique at this stage. The height errors are estimated using the geometric information of the structure. Based on the spatial low-frequency and temporal high-frequency characteristics of the atmospheric phase, the filtering is applied to obtain the nonlinear deformation.

(4) Deformation recovery. The geometric transformation relationship between the radar coordinate system and the geospatial coordinate system is used to obtain the displacement time series of the PS points at the geospatial location of the bridge.

The LOS displacement of the bridge is the sum of the projections of its three-dimensional displacement components onto the LOS direction. Fig. 2 illustrates the SAR side-looking imaging geometry, using descending datasets as an example. The relationship between the LOS deformation and the three-dimensional deformation components is presented as follows:

$$D_{\mathrm{LOS}} = D_{\mathrm{v}} \cdot \cos\theta + D_{\mathrm{n}} \cdot \sin\theta \cdot \sin\alpha - D_{\mathrm{e}} \cdot \sin\theta \cdot \cos\alpha \tag{7}$$

where D_{v}, D_{n}, D_{e} are the displacements in vertical, north-south, and west-east directions respectively. θ is the side-looking angle, α is the azimuth angle, and β is the angle between the bridge and the north-south direction. Considering the deformation orientation of the target point and the spatial geometric imaging relationship of SAR, this relationship can be expressed as follows:

$$D_{\mathrm{LOS}} = D_{\mathrm{v}} \cdot \cos\theta - D_{\mathrm{n}} \cdot \sin\theta \cdot \sin(\alpha+\beta) - D_{\mathrm{e}} \cdot \sin\theta \cdot \cos(\alpha+\beta) \tag{8}$$

Assuming the vertical and transverse displacements are disregarded, the relationship between the longitudinal displacement D_{x} and the LOS displacement can be represented as follows:

$$D_{\mathrm{x}} = D_{\mathrm{LOS}} / \sin\theta \cdot \sin(\alpha+\beta) \tag{9}$$

2.2. Structural temperature field determination

To enhance the calculations accuracy of thermal dilation of the PSI technique, the temperature field of the key structural members at the SAR image acquisition time was used instead of the air temperature. The bridge structural members constantly exchange heat with the environment through thermal convection and radiation. The meteorological parameters required for calculating the temperature field include air temperature, wind speed, and absorbed radiation. The air temperature and wind speed were obtained from the web of WeatherSpark (http://zh . Weatherspark.com). Given the time, location, material properties of the structure, and the normal angles of each surface of the key members, the absorbed radiation can be determined by the Kehlbeck model as follows [39]:

$$I = I_n + I_w + I_r + I_d + I_e \tag{10}$$

$$I_n = I_{sc} 0.9^{(t_u k_a / \sin\beta)} \tag{11}$$

$$I_w = 0.5 I_{sc} \sin\beta \frac{1 - (0.9 t_u k_a)^{(\sin\beta)^{-1}}}{1 - 1.4 \ln(0.9 t_u k_a)} \tag{12}$$

$$I_r = 0.5 r_e (I_n + I_w)(1 - \cos\theta) \tag{13}$$

$$I_d = E_a C_s (T_k + T_a)^4 0.5 (1 - \cos\theta) \tag{14}$$

$$I_e = (E_u / E_a - E_u + 1) I_d \tag{15}$$

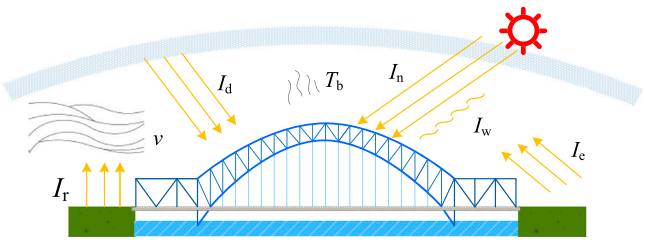

Fig. 3. Thermal environments of a bridge.

whereI_n, I_w, I_r, $I_d$and I_e represent the direct solar radiation, diffuse radiation, ground surface radiation, atmospheric radiation from the sky, and the environmental radiation, respectively; I_{sc} is the solar constant; t_u denotes the turbidity coefficient; k_a is the atmospheric pressure; β represents the solar altitude angle; r_e is the ground radiation coefficient; θ is the angle between the desired surface and the horizontal plane; E_a and E_u are the atmospheric radiation coefficients and environmental radiation coefficients, respectively; C_s represents the blackbody radiation coefficient; T_k is used to convert between Celsius and absolute temperature; T_a is the ambient temperature at bridge location obtained from the weather station data T_{ai} using spatial interpolation method. The

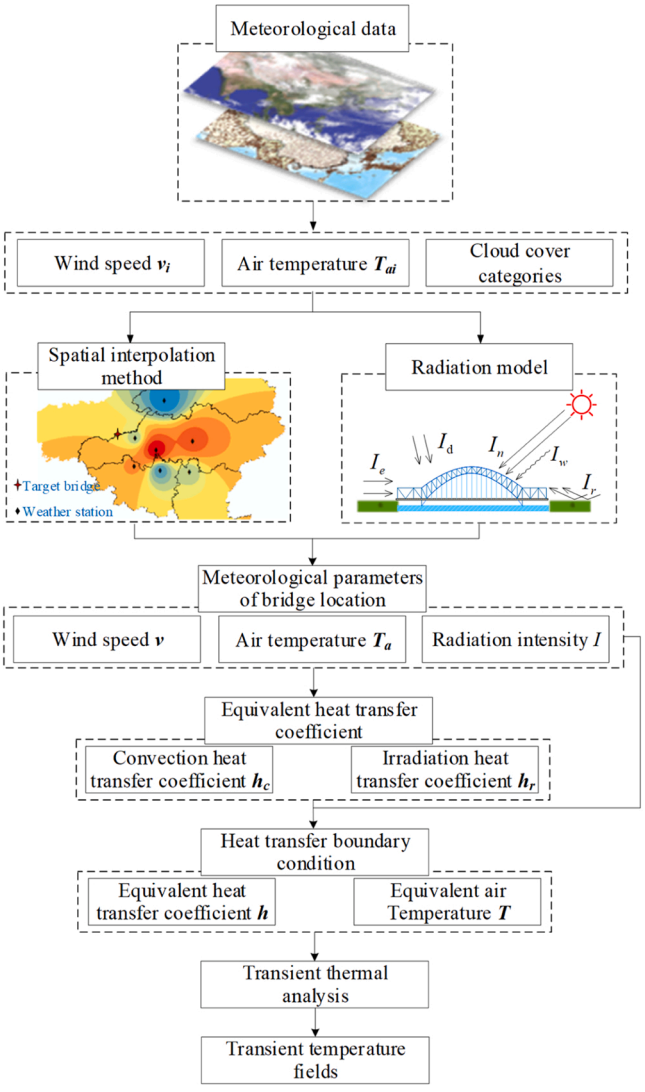

Fig. 4. Bridge temperature field calculation method based on shared meteorological data.

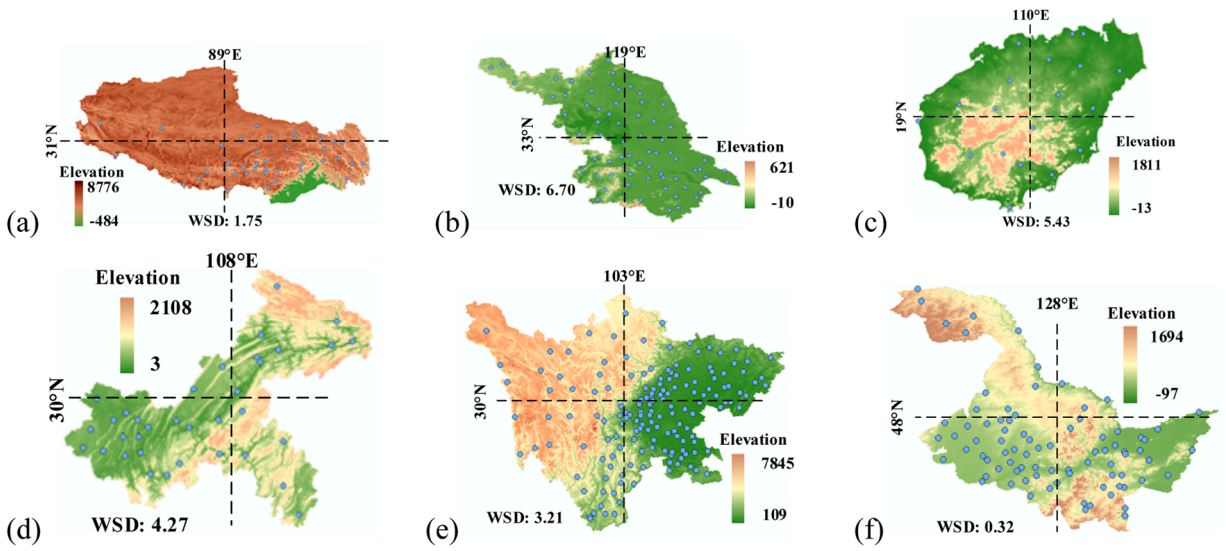

Fig. 5. Topographical maps of different regions (Unit: m). (a) Tibet Autonomous Region; (b) Jiangsu Province; (c) Chongqing Municipality; (d) Sichuan Province; (e) Hainan Province; (f) Heilongjiang Province.

thermal environment is depicted in Fig. 3.

In this study, the Kehlbeck formula was adopted to calculate the convection heat transfer coefficient h_c, while the irradiation heat transfer coefficient h_r was computed using the following empirical formula proposed by Fernando A. Branco [40]:

$$h_c = 5.8 + 4v \tag{16}$$

$$h_r = \varepsilon[4.8 + 0.075(T_a - 5)] \tag{17}$$

where v is the wind speed obtained from the weather station data v_i using spatial interpolation method and ε denotes the emissivity of the structural material.

The heat flux on the boundary is proportional to the difference between the air temperature and the bridge-surface temperature [27]. The boundary conditions for the thermal analysis of a bridge can be written as follows:

$$\lambda \frac{\partial T}{\partial n}\bigg|_s = h(T_a - T_s) \tag{18}$$

where n represents normal to the boundary surface s; h is referred to as equivalent heat transfer coefficient; T_a denotes the air temperature; T_s denotes the structural surface temperature.

$$h = h_c + h_r \tag{19}$$

when considering both radiation and convection loads on the structural members, the radiative heat flux density needs to be equivalently converted to convective heat flux density. The equivalent air temperature at the boundary surface can be expressed as follows:

$$T = T_a + \alpha I/h \tag{20}$$

where α ($0 < \alpha < 1$) represents the absorptivity coefficient of the surface material.

For bridges without adequate temperature sensors installations, on-site measurements could not provide a comprehensive initial temperature of the key structural members. In this study, an initial uniform temperature field was assumed and the equivalent air temperature at sunrise was calculated. The heat transfer boundary conditions were applied to the members. The temperature distribution becomes nonuniform, serving as the initial condition for more detailed thermal analysis.

As depicted in Fig. 4, the equivalent heat transfer boundary conditions, including the equivalent air temperature and the heat transfer coefficient, were employed as convection loads. By conducting a transient thermal analysis, the temperature field of the key structural members was obtained.

Table 1
Spatial interpolation errors for air temperature.

Group	d_{min} (km)	$\bar{d}$ (km)	MAE_{int}	MAE_{nea}	$RMSE_{int}$	$RMSE_{nea}$
A	0-15	36.5	0.63	0.61	0.94	0.94
B	15-20	26.5	0.44	0.38	0.60	0.54
C	20-25	40.5	0.66	0.95	0.90	1.20
D	25-30	56.9	1.06	1.61	1.39	2.03
E	30-35	44.6	0.73	1.05	1.02	1.46

Note: $MAE = \sum_{i=1}^{n}|N_i - M_i|/n$, $RMSE = \sqrt{\sum_{i=1}^{n}(N_i - M_i)^{2/n}}$, N_i represents the actual value; M_i stands for the interpolated value; n is the total number of samples. MAE_{int} and $RMSE_{int}$ denote the indictors derived from interpolated results, while MAE_{nea} and $RMSE_{nea}$ are those from the nearest weather station.

2.3. Meteorological data calculation

Based on meteorological data from weather stations, calculations for the bridge location were performed using the inverse square distance gradient method [41] for air temperature and the Kriging method [42] for wind speed. The performance of interpolation methods was evaluated, leading to a strategy for computing meteorological data at varying straight-line distances between the bridge and the weather stations. Six representative regions were evaluated - Tibet Autonomous Region, Jiangsu Province, Chongqing Municipality, Sichuan Province, Hainan Province, and Heilongjiang Province - considering factors such as longitude, latitude, altitude, weather stations density, and topography. The topographical maps are shown in Fig. 5.

Based on the hourly air temperature observed by ground meteorological stations in various regions from February 15 to February 25, 2023, the distance d between the target meteorological station and the nearest station was used as the classification criterion. A total of 401 ground meteorological stations distributed in these regions were divided into six groups. Taking a meteorological station as the target location, the spatial interpolation methods were performed using temperature or wind speed data from the five nearest meteorological stations. The interpolated results at the target location for temperature are shown in

Table 2
Spatial interpolation errors for wind speed.

Group	d_{min} (km)	$\overline{d}$ (km)	MAE_{int}	MAE_{nea}	$RMSE_{int}$	$RMSE_{nea}$
A	0-15	36.5	0.90	0.94	1.13	1.19
B	15-20	26.5	0.65	0.65	0.81	0.86
C	20-25	40.5	0.82	1.00	1.05	1.26
D	25-30	56.9	0.80	1.00	1.03	1.28
E	30-35	44.6	0.72	0.86	0.92	1.10

Table 1, and for wind speed in Table 2. The mean absolute error (MAE) and root mean squared error (RMSE) are used to assess the accuracy of the spatial interpolation methods. The interpolated errors for air temperature and wind speed are influenced by the spatial distribution of the weather stations. Particularly, the distance from the target location to the nearest station d_{min} and the average distance to the stations $\overline{d}$.utilized for interpolation play a significant role. It can be found that if $d_{min}$was less than 20 km, the MAE derived from using temperature or wind speed values from the closest meteorological station is lower than that obtained from interpolated predictions using surrounding stations. Consequently, if d_{min} is under 20 km, it's advisable to directly use the air temperature or the wind speed from that nearest station for the target location.

3. Deflection of case study bridge

3.1. Details of case study bridge

A six-lane high-speed railway bridge was used as a case study, which consists of two continuous steel-truss arches and four approach spans, with a span configuration of 108 + 192 + 336 + 336 + 192 + 108 m. The overall layout of the bridge is shown in Fig. 6. Spherical steel bearings are used as supports, with the #7 being a fixed support, and the other supports allowing longitudinal motion as movable bearings. Since the bridge piers has deep pile foundations, vertical settlement is virtually negligible [43,44] and as the lateral displacement was found to be less than 1 % of the longitudinal displacement it was ignored in the subsequent analysis [45]. Hence, the displacements caused by the temperature were observed at the bridge's piers along the longitudinal direction.

3.2. SAR datasets

A total of 163 scenes of S1A interferometric wide swath imagery with a resolution of 5 m × 20 m (ascending orbit) from January 2017 to December 2021 were used, and 35 scenes of CSK spotlight imagery with a resolution of 1.2 m × 1.9 m (descending orbit) from September 2016 to September 2019 were also utilized. The temporal and spatial baselines of the images are illustrated in Fig. 7. For the S1A satellite, the incidence angle, denoted as θ_1, is 33.91°, and its corresponding heading angle, represented as α_1, is 349.26°. Similarly, the CSK satellite has a 33.94° incidence angle, designated as θ_2, and its associated heading angle, denoted as α_2, is 190.55°. The bridge's longitudinal axis is oriented at a 45° angle to true north. The selected S1A and CSK image capture times were 10:03 and 09:53 respectively. The bridge is in the UTC+ 8 time zone and the SAR image time is around 18:00.

3.3. Meteorological data

To compute meteorological parameters, the study utilized hourly temperature and wind speed data obtained from an airport weather station near the case study bridge, which were accessed through the WeatherSpark platform. Since the case study bridge was located 16 kilometers in a straight line from the airport, the ambient temperature at the airport can be assumed to be representative of that at the bridge location. The meteorological parameters of ambient temperature and average wind speed were recorded at the airport weather station from

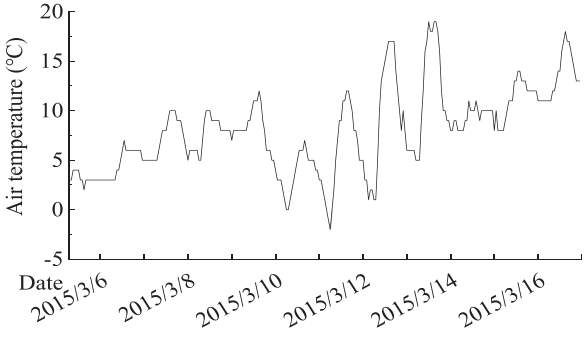

Fig. 8. Ambient temperature.

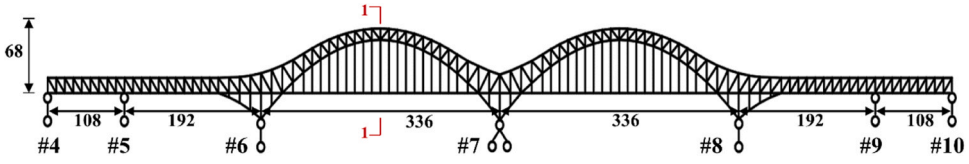

Fig. 6. Layout of the case study bridge (Unit: m).

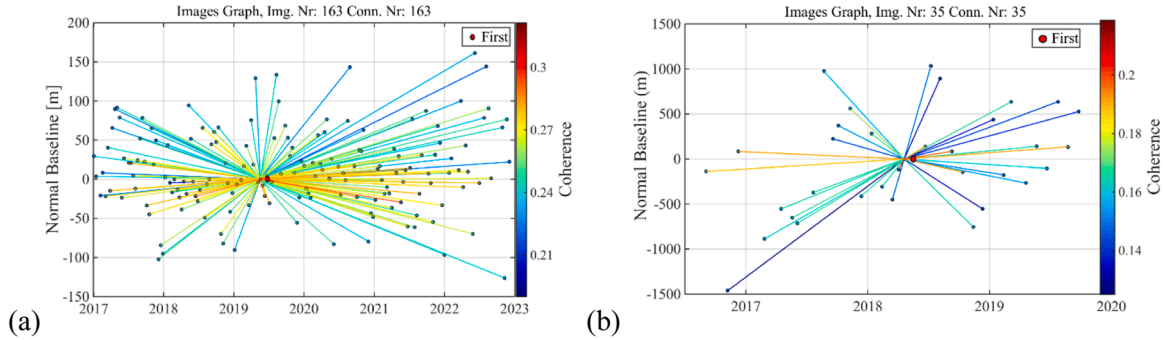

Fig. 7. Perpendicular baseline vs temporal baseline plot. (a) S1A; (b) CSK.

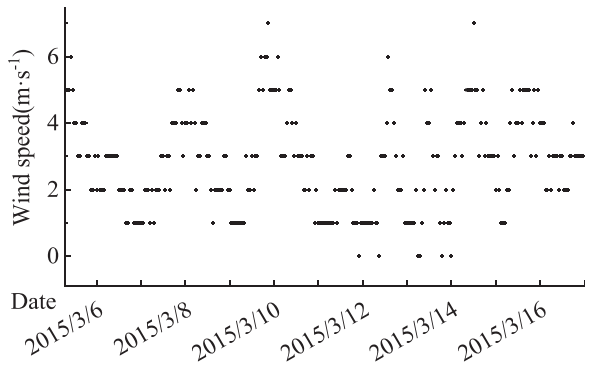

Fig. 9. Wind speed.

March 5th to 16th, 2015 (as depicted in Fig. 8 and Fig. 9), and used for calculating the structural temperature field. Additionally, fiber Bragg grating temperature sensors were installed as illustrated in Fig. 10 [46].

3.4. Solar radiation and deck shading

Fluctuations in the surface azimuth angle, solar altitude angle, and projection angle induce alterations in the illuminated and shaded regions on a structure's surface [47]. Taking January 1, 2020, as an example, sunrise is at 7:04 am, and sunset is at 5:11 pm. By analyzing the positional relationship between the solar trajectory and the bridge deck, the bearings of side truss were exposed to sunlight from 7:04 am to 11:27 am. Afterward, they remained in the shaded area until 5:11 pm, as illustrated in Fig. 11(a). The bearing of mid-truss was covered by the bridge deck and truss members in the whole daytime, as depicted in Fig. 11(b). Hence, the solar radiation was utilized to address the

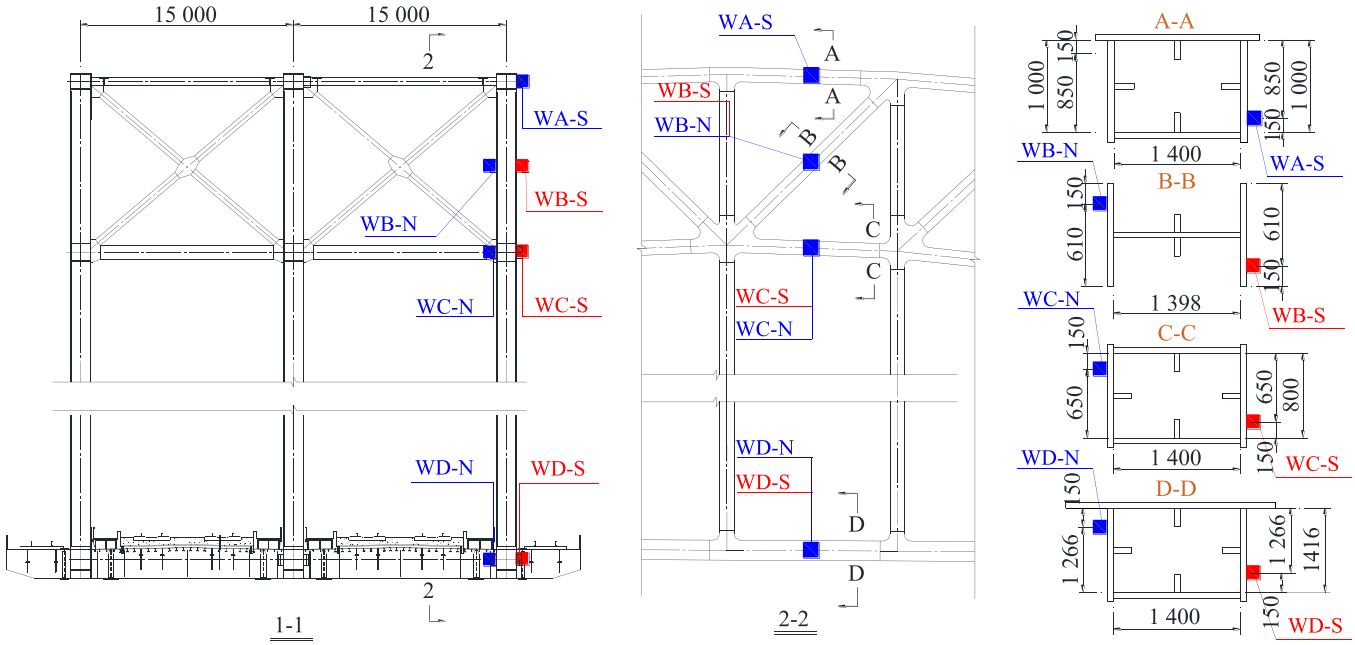

Fig. 10. Location of temperature sensors (unit: mm).

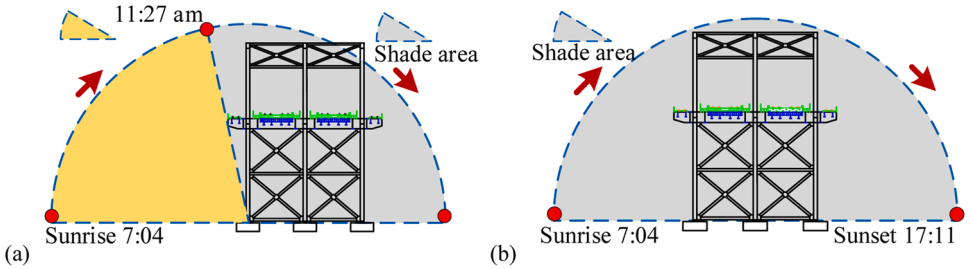

Fig. 11. Description of solar motion and deck shading. (a) bearing of side main truss; (b) bearing of middle main truss.

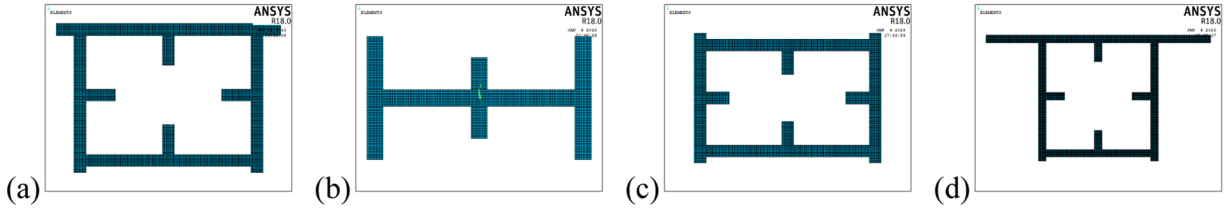

Fig. 12. FE model of key members. (a) section A-A; (b) section B-B; (c) section C-C; (d) section D-D.

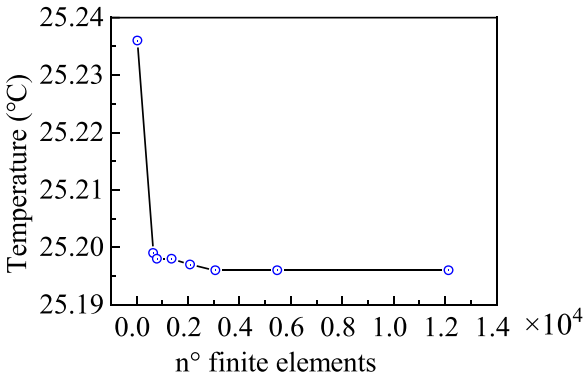

Fig. 13. Temperature variation with the number of finite elements.

influence of shadow on the structure's surface caused by the sun's motion.

4. Application of the PSI technique refined by temperature field

4.1. Thermal analysis of the box-shaped cross section and Convergence analysis

The temperature distribution in the bridge's longitudinal direction is assumed to remain uniform [48]. The two-dimensional FE models of the truss members' cross-sections were constructed using the PLANE55 element in ANSYS 2021 R1, which possesses four temperature degrees of freedom at its nodes. The steel material is Q345qD, with a thermal conductivity of 60.5 W/(m·℃) and a heat capacity of 434 J/(kg·℃). See Fig. 12.

The chosen mesh must ensure solution convergence for the heat diffusion problem. And the section A-A FE model in Fig. 12 was selected to analyze the convergence. The solution's behavior as a function of the number of finite elements is valuable for determining the threshold mesh density for convergence. Fig. 13 illustrates the mesh configurations with varying numbers FEs. For the thermal problem, considering the two-dimensional FE model's average temperature at 8:00 pm on March 9, 2015, as a representative solution parameter is essential. The solutions show monotonic convergence with an increase in the number of FEs, reaching a point beyond which additional increases in mesh density no longer influence the result. By adopting around 0.6 × 104 FEs, solution convergence for both issues are secured [49,50].

The material properties for thermal analysis and the equivalent heat transfer boundary conditions were input into the established FE model. The time-dependent temperature curves were then obtained as shown in Fig. 14. The comparison between the measured and calculated values indicates a consistent trend with an average error ranging from − 2.56 % to 2.50 %. This discrepancy arises from two primary sources. Firstly, the temporal variability of wind speed, influenced by factors such as environmental obstructions, local temperature differences, and the geographical landscape, contributes to the error in temperature calculations. Secondly, the precision of solar radiation intensity calculations, significantly affected by climatic conditions like cloud cover and humidity, also plays a crucial role in the observed temperature deviations.

4.2. Bridge FE model analysis

A three-dimensional FE model of the case study bridge is established to analyze the bridge deflection under various temperatures. As shown in Fig. 15, the bridge FE model consists of 59,918 nodes and 112,706 elements. The trusses, hangers, and stiffeners are established by a BEAM188 element, and the steel decks and the diaphragms of the box girder are established by a SHELL181 element. The boundary conditions

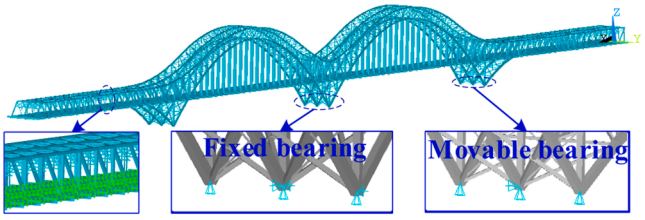

Fig. 15. Bridge FE model.

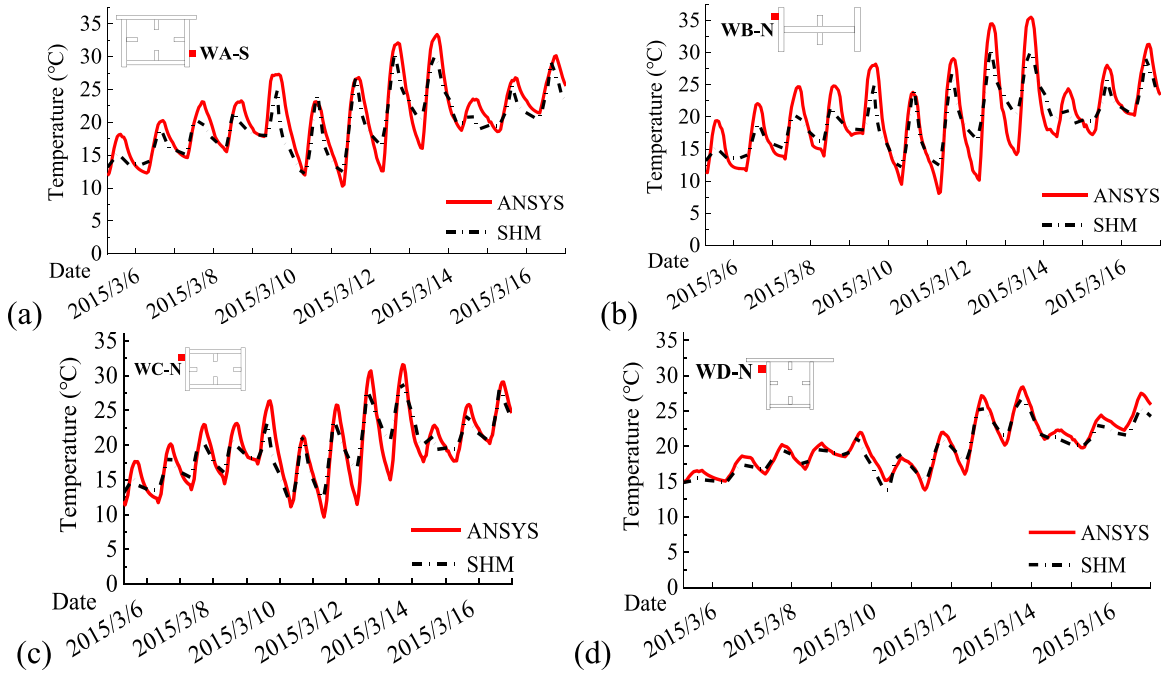

Fig. 14. Temperature time history curves. (a) WA-S; (b) WB-N; (c)WC-N; (d) WD-N.

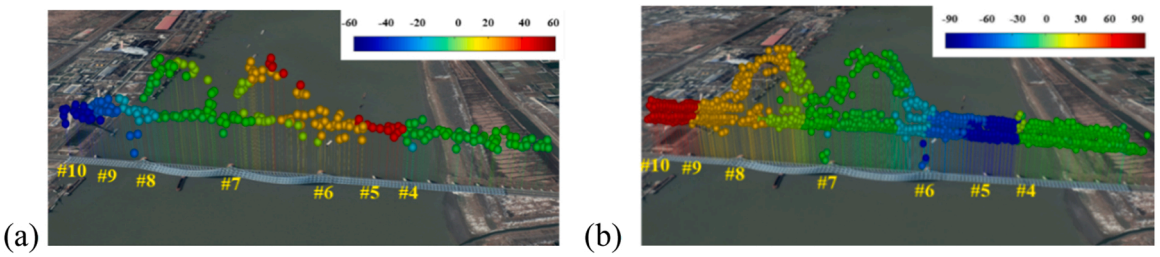

Fig. 16. Spatial distribution and LOS deformation of PS points (mm/year). (a) S1A, (b) CSK.

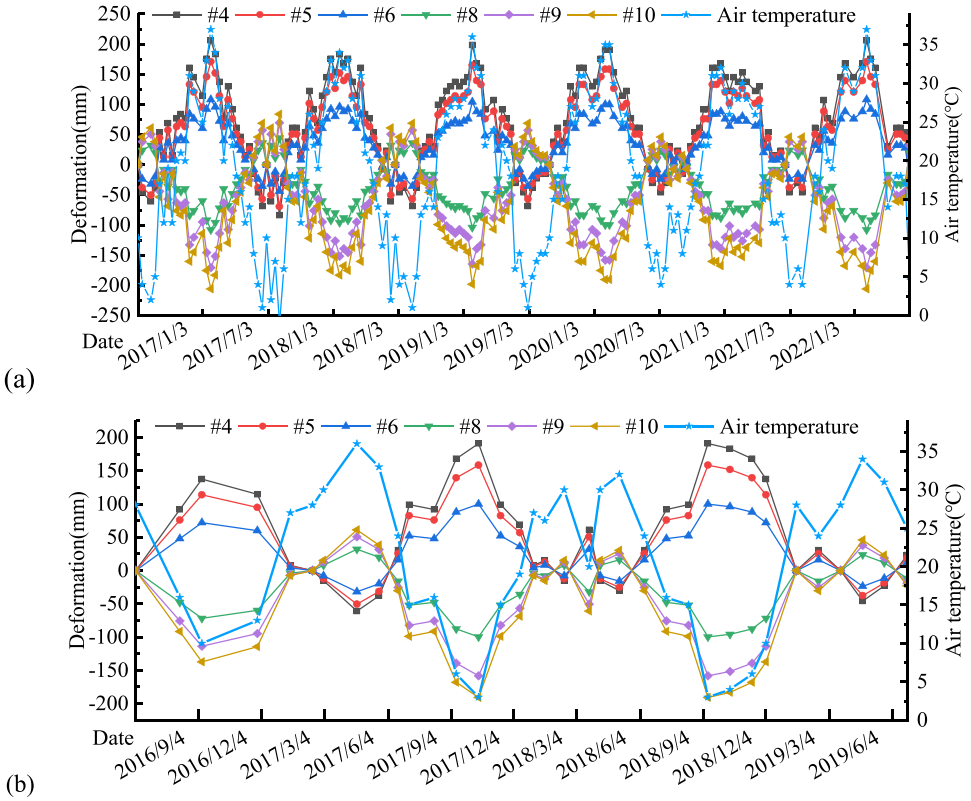

Fig. 17. LOS deformation at six piers and image acquisition temperatures. (a) S1A; (b) CSK.

of the FE model are set as follows: the boundary conditions of the 7# piers are restrained with all translational degrees of freedom including longitudinal X, transverse Y, and vertical Z, and the boundary conditions at remaining piers are restrained in the Z-direction and Y-direction. Moreover, the thermal expansion coefficients of the FE model were set as 1.2×10^{-5}/℃. Based on the heat transfer boundary conditions, the materials' thermal conductivity and heat capacity, the temperature fields of the truss members were determined through the principles of heat transfer theory. The time-dependent temperatures of these members were treated as loads and applied to the bridge FE model. The temperature-induced deformation was then obtained by transient thermal analysis.

4.3. RPSI-derived displacement time series

The temperature field of the structural members were obtained through transient thermal analysis as mentioned in Section 4.1. Consequently, the temperature of the bridge's PS points at the SAR image acquisition time can be employed in Eq. (3) and Eq. (6) for differential interferometric processing. Leveraging the time-dependent temperature distributions has enhanced the calculation accuracy of the thermal dilation phase, thereby improving the measurement precision of RPSI-based LOS deformation. The LOS deformation velocity of the bridge's PS points is shown in Fig. 16. The spatial distribution of PS points, based on both CSK and S1A data, aligns well with the bridge's geometric shape. The deformation velocity displays evident symmetry with respect to the #7 support. The deformation time series at each pier and the air temperature at the image acquisition time are presented in Fig. 17. There is a strong correlation between the LOS deformation and air temperature, indicting distinct periodic characteristics. The deformation time series at piers #4 to #6 show a positive correlation with air temperature, while piers #8 to #10 exhibit the opposite correlation. Additionally, the deformation at six piers displays symmetric characteristics relative to the central symmetry of pier #7.

4.4. Comparison of the InSAR-measured and simulated displacement

The time-dependent temperature of the key members cross-section was applied to the nodes of the FE model (bottom surface of the deck slab, longitudinal and transverse beams, top chord, web members, and bottom chord) to obtain the bridge deformation under various temperatures. Based on the LOS deformation discussed in Section 4.2, the longitudinal displacement at six piers was derived using Eq. (9). This displacement was then compared with the simulated results, as depicted

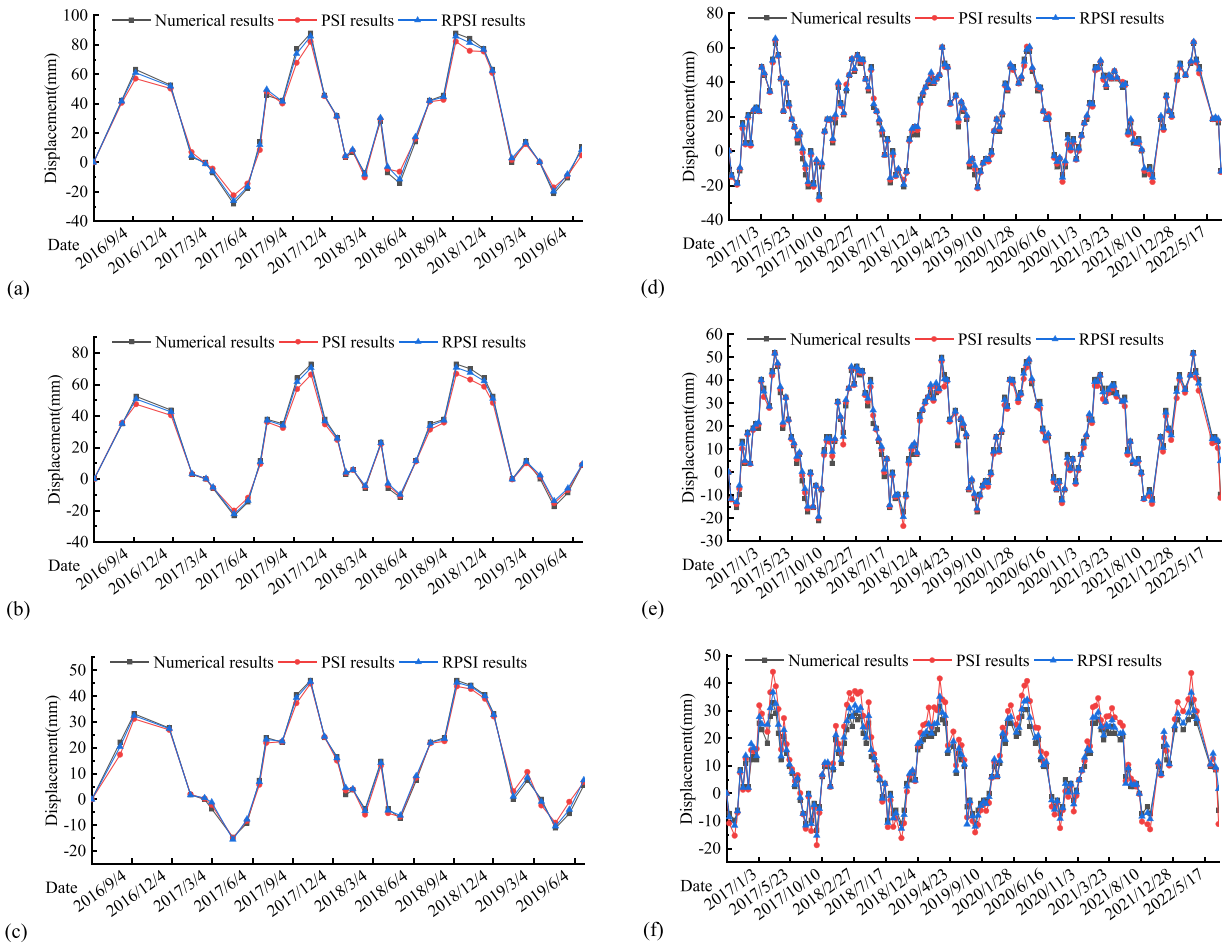

Fig. 18. InSAR-measured and simulated longitudinal displacement. (a) #4, CSK; (b) #5, CSK; (c) #6, CSK; (d) #4, S1A; (e) #5, S1A; (f) #6, S1A.

Table 3
Comparison of longitudinal displacement calculation error (mm).

Piers	S1A			CSK		
	#4	#5	#6	#4	#5	#6
MAE_{PSI}	1.43	1.66	4.11	3.07	2.38	1.75
MAE_{RPSI}	1.16	1.12	1.74	1.59	1.24	1.06
$RMSE_{PSI}$	1.84	1.92	4.45	3.91	3.15	1.94
$RMSE_{RPSI}$	1.69	1.86	2.18	1.93	1.56	1.08
$MaxAE_{PSI}$	5.58	24.57	19.65	9.49	7.58	4.73
$MaxAE_{RPSI}$	6.09	14.48	9.67	4.15	3.54	2.67

Note:MAE $= \frac{1}{n}\sum_{i=1}^{n}|y_i - \hat{y}_i|$, RMSE $= \sqrt{\frac{1}{n}\sum_{i=1}^{n}(y_i - \hat{y}_i)^2}$, and MaxAE $= \max_i|y_i - \hat{y}_i|$, where y_i represents the numerical results. $\hat{y}_i$ denotes the InSAR-based results, and n is the total number of SAR acquisition.

in Fig. 18. It is noticeable that both PSI and RPSI measured results are in good agreement with the simulated results, with RPSI technique demonstrating higher accuracy. The errors in longitudinal displacement measurement, derived from the processing of the CSK and S1A data using both PSI and RPSI techniques, are listed in Table 3. Compared to the numerical results, the MAE of the RPSI-derived displacement measurements is consistently lower than that of PSI technique. Similarly, RMSE associated with the RPSI method is also less than that of the PSI technique, which is particularly evident when considering the maximum absolute error (MaxAE). For both S1A and CSK datasets, the error for PSI technique ranges from 4.73 mm to 24.57 mm, whereas for RPSI technique, it lies between 2.67 mm and 14.48 mm. This investigation demonstrates that by utilizing shared meteorological data and employing thermal analysis methods to determine the structural temperature at the location of bridge's PS points during SAR imaging, the calculation precision of the thermal expansion phase can be effectively refined, leading to enhanced deformation measurement accuracy of the PSI technique. In addition, despite the relatively lower spatial resolution of S1A imagery compared to CSK imagery, the calculated results reveal a comparable level of displacement measurement accuracy for both datasets. Considering that S1A imagery can be freely accessed from platforms such as National Aeronautics and Space Administration (NASA), United States Geological Survey (USGS), and European Space Agency (ESA), it presents an economically and reasonably accurate method for long-term bridge deformation monitoring using the RPSI technique. The results of this study confirm that the RPSI technique stands as a viable and effective approach for lightweight bridge monitoring, meeting engineering accuracy requirements.

4.5. Comparison of InSAR and field measurement

To further validate the accuracy of deformation measured using RPSI technique, the long-term correlation was analyzed between longitudinal displacement at the piers and ambient temperature. Moreover, the deformation calculation accuracy of the RPSI technique and the conventional PSI technique was compared. Using both the PSI and RPSI techniques to process the SIA and CSK data, the longitudinal displacement of the case study bridge piers has been determined. This displacement exhibits a high linear correlation with the ambient temperature, as illustrated in Fig. 19. This figure presents four scenarios: S1A data processed with the PSI technique (S1A-PSI), CSK data

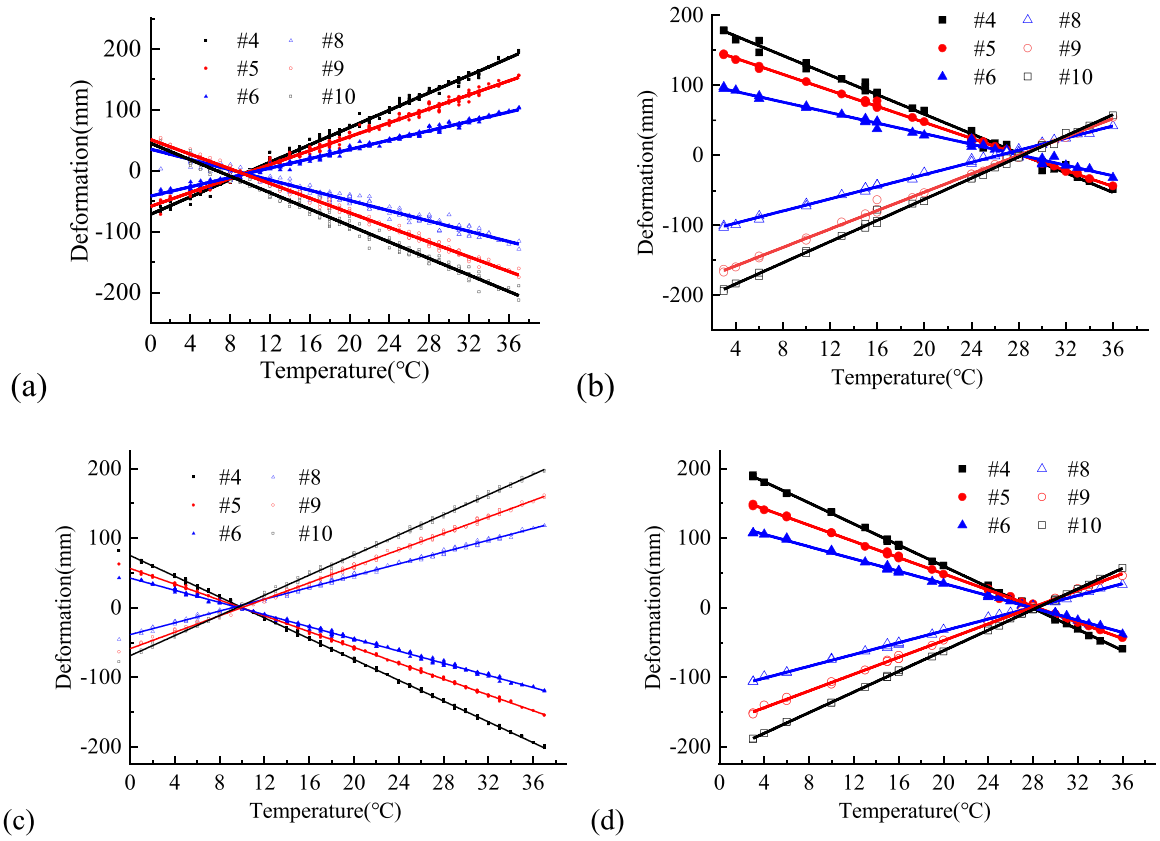

Fig. 19. Linear regression model of the longitudinal displacements with respect to the ambient temperatures. (a) S1A-PSI; (b) CSK-PSI; (c) S1A-RPSI; (d) CSK-RPSI.

Table 4
Comparison of thermal dilation velocity (mm/℃).

Piers	#4	#5	#6	#8	#9	#10
Field data	7.23	6.05	4.21	4.42	6.12	6.96
S1A-PSI	7.12	6.14	3.74	3.85	5.80	6.82
CSK-PSI	6.99	5.72	3.76	4.34	6.58	7.56
S1A-RPSI	7.47	5.68	4.37	4.24	5.92	7.23
CSK-RPSI	7.56	5.82	4.40	4.22	6.01	7.19
$E_{S1A\text{-}PSI}$	-2.01 %	3.28 %	-11.16 %	-12.90 %	-5.26 %	-2.04 %
$E_{CSK\text{-}PSI}$	-1.83 %	-3.78 %	-10.69 %	-1.81 %	7.48 %	8.62 %
$E_{S1A\text{-}RPSI}$	2.81 %	-4.46 %	3.80 %	-4.07 %	-3.30 %	3.85 %
$E_{CSK\text{-}RPSI}$	4.05 %	-2.10 %	4.51 %	-4.52 %	-1.83 %	3.30 %

Note: The term "Field data" refers to TDV derived from on-site displacement measurements as reported in literature [40]. The equation for relative error of the TDV calculation is given by E = (dI – dF)/dF, where dF indicates the TDV from field data and dI denotes the TDV calculated using an InSAR-based method, i.e., PSI or RPSI technique.

processed with the PSI technique (CSK-PSI), S1A data processed with the RPSI technique (S1A-RPSI), and CSK data processed with the RPSI technique (CSK-RPSI). It is clear that the thermal dilation velocity (TDV) (displacement caused by unit air temperature change), as represented by the slope of the temperature-fitted curve for longitudinal displacement, is smaller at the support near pier #7 and larger for those located farther from pier #7. The TDV obtained from RPSI and PSI technique is summarized in Table 4. For the PSI technique, the errors in calculating longitudinal displacement range from – 12.90 % to 3.28 % with S1A data and – 10.69 to – 8.59 % with CSK data. For the RPSI technique, the associated errors span from – 4.07 % to 3.85 % using S1A data and – 4.52 % to 4.50 % using CSK data. The computational results demonstrate that RPSI exhibits enhanced accuracy in displacement measurement, attributed to the thermal dilation phase refined by the temperature field of the structural members. It's worth noting that the spatial distributed discrepancy between the on-site installed sensors and the PS points could be a significant source of errors in the displacement measurements.

This study revealed that the thermal dilation phase primarily affects the accuracy of PSI technique in the measurement of bridge deformation. Given that the focus of this investigation is on a steel-truss arch bridge, it is generally understood that the rates of heat convection and radiation surpass those in concrete box girder bridges. Consequently, in the case of concrete steel box girder bridges, the discrepancy between the bridge's temperature field and the ambient temperature becomes more pronounced thereby renders the use of RPSI technology particularly advantageous for deformation monitoring. Currently, research focused on improving the accuracy of PSI technique remains scarce. The proposed RPSI method serves as an effective tool for assessing bridge deformation, acknowledging the variations between air temperature and the bridge's temperature field. The findings from this study serve as a valuable reference for lightweight monitoring of long-span bridges through InSAR technology.

5. Conclusions

This study focused on utilizing the InSAR technique for displacement measurements of a steel-truss arch bridge. By utilizing the meteorological sharing data and heat-transfer analysis method, the time-dependent temperature of the bridge members was obtained. The members' temperature was instrumental in refining the thermal dilation phase calculation, thereby enhancing the accuracy of bridge deformation monitoring using the RPSI technique. The main conclusions are as follows.

(1) The temperature field was obtained without field monitoring data by using meteorological sharing data. The heat transfer boundary conditions of the structure were determined using

meteorological parameters such as the bridge's geographical coordinates, material emissivity, air temperature, and wind speed. With the boundary conditions, thermal conductivity and heat capacity of the members' material, the temperature-time curves were derived from transient thermal analysis.

(2) The accuracy of deformation monitoring using the RPSI technique can be effectively refined by the bridge temperature field. Thermal dilation is a critical component of the RPSI-based bridge deformation. The computational accuracy was improved by adopting time-dependent temperature instead of ambient air temperatures, thereby enhancing the precision of measurements obtained with the RPSI technique.

(3) The RPSI technique was employed to analyze the S1A and CSK data to depict the bridge's spatiotemporal deformation. Temporally, a strong correlation emerged between LOS displacement and air temperature. Spatially, the maximum longitudinal displacement caused by a unit temperature change was observed at piers #4 and #10.

(4) Compared to numerical results, the MAE and RMSE values from the RPSI technique were both lower than those from the PSI technique, confirming the enhanced accuracy of RPSI in deformation monitoring. Moreover, despite the relatively lower spatial resolution of S1A imagery, the derived measurements demonstrate that the displacement detection accuracy of S1A is comparable to CSK datasets.

(5) The TDV derived from both the RPSI and PSI techniques was compared to field measurements. For S1A and CSK data, the TDV relative error ranged from − 12.9 % to 8.59 % using the PSI technique, while the TDV relative error using the RPSI technique ranged from − 4.52 % to 4.50 %, validating the superior performance of the RPSI technique over the PSI technique.

The accuracy of deformation measurement using conventional PS-InSAR technology is well refined with a structural temperature field. Consequently, the proposed RPSI technique provides a powerful tool for achieving lightweight and non-contact structural health monitoring in future.

CRediT authorship contribution statement

Jiayuan Zheng: Visualization, Validation, Methodology. **Junjie Wei:** Validation, Methodology, Investigation. **JianWei Chen:** Validation, Investigation, Data curation. **Guanwang Hao:** Writing – original draft, Visualization, Validation, Software, Project administration, Methodology, Conceptualization. **Yun Zhou:** Writing – review & editing, Supervision, Resources, Project administration, Funding acquisition, Conceptualization.

Declaration of Competing Interest

The authors declare that they have no conflict of interest.

Data availability

Data will be made available on request.

Acknowledgements

The authors sincerely appreciate the funding support provided by the National Natural Science Foundation of China (NSFC) (No.52278306), the Key Research and Development Program of Hunan Province (No. 2022SK2096), the Hunan Provincial Natural Science Foundation of China (No. 2023JJ70003), and the Science and Technology Progress and Innovation Project of Department of Transportation of Hunan Province (No.201912). We are grateful to Jiping Li and Mao Zhu for providing CSK satellite imagery and sharing their experience in InSAR data processing. The Sentinel-1A data were downloaded from the Alaska Satellite Facility Data Search.

References

[1] Bonopera M, Chang KC, Chen CC, Lee ZK, Sun YC, Tullini N. Fiber Bragg grating–differential settlement measurement system for bridge displacement monitoring: case study. J Bridge Eng 2019;24(10):1–12.
[2] Zhang LX, Liu P, Yan X, Zhao XF. Middle displacement monitoring of medium–small span bridges based on laser technology. Struct Control Health Monit 2020;27(4):e2509.
[3] Infante D, Di M, Diego, Confuorto P, Tessitore S, Tòmas R, et al. Assessment of building behavior in slow-moving landslide-affected areas through DInSAR data and structural analysis. Eng Struct 2019;199:109638.
[4] Perissin D, Wang Z, Lin H. Shanghai subway tunnels and highways monitoring through Cosmo-SkyMed Persistent Scatterers. ISPRS J Photo Remote Sens 2012;73:58–67.
[5] Macchiarulo V, Milillo P, Blenkinsopp C, Giardina G. Monitoring deformations of infrastructure networks: a fully automated GIS integration and analysis of InSAR time-series. Struct Health Monit 2022;21(4):1849–78.
[6] Emadali L, Motagh M, Haghshenas MH. Characterizing post-construction settlement of the Masjed-Soleyman embankment dam, Southwest Iran, using TerraSAR-X SpotLight radar imagery. Eng Struct 2017;143:261–73.
[7] Huang QH, Crosetto M, Monserrat O, Crippa B. Displacement monitoring and modelling of a high-speed railway bridge using C-band Sentinel-1 data. Isprs J Photogramm Remote Sens 2017;128(1)):204–11.
[8] Ma PF, Li T, Fang CY, Lin H. A tentative test for measuring the sub-millimeter settlement and uplift of a high-speed railway bridge using COSMO-SkyMed images. ISPRS J Photo Remote Sens 2019;155:1–12.
[9] Qin XQ, Ding XL, Liao MS. Capturing the deformation characteristics of cable-stayed bridges with multi-temporal SAR interferometry. In: Proceedings of the fifth international workshop on earth observation and remote sensing applications (EORSA). Xian, CHN,; 2018.
[10] Caspani VF, Tonelli D, Rocca A, Torboli R, Vitti A, Zonta D. Satellite InSAR technology for structural health monitoring of road bridges and the surrounding territory: a case study. In: Proceedings of the conference on sensors and smart structures technologies for civil, mechanical, and aerospace systems. CA, USA 2023.
[11] Farneti E, Cavalagli N, Costantini M, Trillo F, Minati F, Venanzi I, et al. Remote sensing satellite data and progressive collapse analysis for structural monitoring of multi-span bridges. In: Proceedings of the tenth European workshop on structural health monitoring (EWSHM). Palermo; 2022.
[12] Sousa JJ, Bastos L. Multi-temporal SAR interferometry reveals acceleration of bridge sinking before collapse. Nat Hazard Earth Syst 2013;13(3):659–67.
[13] Milillo P, Giardina G, Perissin D, Milillo G, Coletta A, Terranova C. Pre-collapse space geodetic observations of critical infrastructure: the Morandi Bridge, Genoa, Italy. Remote Sens 2019;11(12):1403.
[14] Hoppe EJ, Novali F, Rucci A, Fumagalli A, Del Conte S, Falorni G, et al. Deformation monitoring of posttensioned bridges using high-resolution satellite remote sensing. J Bridge Eng 2019;24(12):04019115.
[15] Farneti E, Cavalagli N, Venanzi I, Salvatore W, Ubertini F. Residual service life prediction for bridges undergoing slow landslide-induced movements combining satellite radar interferometry and numerical collapse simulation. Eng Struct 2023;293:116628.
[16] Fornaro G, Reale D, Verde S. Bridge thermal dilation monitoring with millimeter sensitivity via multidimensional SAR imaging. IEEE Geosci Remote Sens 2013;10(4):677–81.
[17] Jung J, Kim DJ, Vadivel P, Yun SH. Long-term deflection monitoring for bridges using X and C-band time-series SAR interferometry. Remote Sens 2019;11(11):1258.
[18] Cusson D, Rossi C, Ozkan IF. Early warning system for the detection of unexpected bridge displacements from radar satellite data. J Civ Struct Health Monit 2021;11(1):189–204.
[19] Lazecky M, Hlavacova I, Bakon M, Sousa JJ, Perissin D, Patricio G. Bridge displacements monitoring using Space-Borne X-Band SAR interferometry. IEEE J-STARS 2017;10(1):205–10.
[20] Qin XQ, Liao MS, Zhang L, Yang MS. Structural health and stability assessment of high-speed railways via thermal dilation mapping with time-series InSAR analysis. IEEE J STARS 2017;10(6):2999–3010.
[21] Qin XQ, Zhang L, Yang MS, Luo M, Liao MS, Ding XL. Mapping surface deformation and thermal dilation of arch bridges by structure-driven multi-temporal DInSAR analysis. Remote Sens Environ 2018;216:71–90.
[22] Huang SJ, Cai CZ, He XH, Li C. Comparison of the corrugated steel web composite box-girder and traditional girders regarding temperature field under solar radiation. Eng Struct 2023;291:116419.
[23] Fan JS, Liu YF, Liu C. Experiment study and refined modeling of temperature field of steel-concrete composite beam bridges. Eng Struct 2021;240:112350.
[24] Tao TY, Wang H, Zhu QX, Zou ZQ, Li J, Wang LB. Long-term temperature field of steel-box girder of a long-span bridge: measurement and simulation. Eng Struct 2021;236:111924.
[25] Xu YL, Chen B, Ng CL, Wong KY, Chan WY. Monitoring temperature effect on a long suspension bridge. Struct Control Health Monit 2010;17(6):632–53.
[26] Lu Y, Li D, Wang K, Jia SW. Study on solar radiation and the extreme thermal effect on concrete box girder bridges. Appl Sci-Basel 2021;11(14):6332.

[27] Zhou LR, Xia Y, Brownjohn JMW, Koo KY. Temperature analysis of a long-span suspension bridge based on field monitoring and numerical simulation. J Bridge Eng 2016;21(1):04015027.
[28] Xia Y, Chen B, Zhou XQ, Xu YL. Field monitoring and numerical analysis of Tsing MA Suspension Bridge Temperature Behavior. Struct Control Health Monit 2013; 20(4):560–75.
[29] Tomé ES, Pimentel M, Figueiras J. Structural response of a concrete cable-stayed bridge under thermal loads. Eng Struct 2018;176:652–72.
[30] Xia Q, Liu SL, Zhang J. Temperature analysis of a long-span suspension bridge based on a time-varying solar radiation model. Smart Struct Syst 2020;25(1): 23–35.
[31] Fan JS, Li BL, Liu C, Liu YF. An efficient model for simulation of temperature field of steel-concrete composite beam bridges. Structures 2022;43:1868–80.
[32] Wang ZW, Zhang WM, Zhang YF, Liu Z. Temperature prediction of flat steel box girders of long-span bridges utilizing in situ environmental parameters and machine learning. J Bridge Eng 2022;27(3):04022004.
[33] Xia Q, Wu WL, Li FN, Zhou XQ, XuYL, Xia Y. Temperature behaviors of an arch bridge through integration of field monitoring and unified numerical simulation. Adv Struct Eng 2022;25(16):3492–509.
[34] Li LF, Shan YS, Jing Q, Yan Y, Xia ZL, Xia Y. Global temperature behavior monitoring and analysis of a three-tower cable-stayed bridge. Eng Struct 2023;295: 116855.
[35] Abid SR, Tayi N, Zaka M. Experimental analysis of temperature gradients in concrete box-girders. Constr Build Mater 2016;106:523–32.
[36] Lu HL, Hao J, Zhong JW, Wang YF, Yang HY. Analysis of sunshine temperature field of steel box girder based on monitoring data. Adv Civ Eng 2020;2020(3): 9572602.
[37] Ferretti A, Prati C, Rocca F. Permanent scatterers in SAR interferometry. IEEE Trans Geosci Remote Sens 2001;39(1):8–20.
[38] Hooper A, Bekaert D, Spaans K, Arikan M. Recent advances in SAR interferometry time series analysis for measuring crustal deformation. Tectonophysics 2012;514: 1–13.
[39] Elbadry MM, Ghali A. Temperature variations in concrete bridges. J Struct Eng 1983;109(10):2355–74.
[40] Branco FA, Mendes PA. Thermal actions for concrete bridge design. J Struct Eng 1993;119(8):2313–31.
[41] Nalder IA, Wein RW. Spatial interpolation of climatic normals: test of a new method in the Canadian boreal forest. Agr Meteor 1998;92(4):211–25.
[42] Cressie N. The origins of kriging. Math Geol 1990;22(3):239–52.
[43] Xia CY, Zhong TY. Numerical analysis of the Nanjing Dashengguan Yangtze River Bridge subjected to non-uniform seismic excitations. J Mech Sci Technol 2011;25 (5):1297–306.
[44] Zhao HW, Ding YL, Nagarajaiah S, Li AQ. Longitudinal displacement behavior and girder end reliability of a jointless steel-truss arch railway bridge during operation. Appl Sci 2019;9(11):2222.
[45] Ding YL, Wang GX, Sun P, Wu LY, Yue Q. Long-term structural health monitoring system for a high-speed railway bridge structure. Sci World J 2015;2015:250562.
[46] Wang GX, Ding YL, Song YS, Wu LY, Yue Q, Mao GH. Detection and location of the degraded bearings based on monitoring the longitudinal expansion performance of the main girder of the Dashengguan Yangtze Bridge. J Perform Constr Fac 2016;30 (4):04015074.
[47] Wang GX, Zhou X, Ding YL, Liu XW. Long-term monitoring of temperature differences in a steel truss bridge with two-layer decks compared with bridge. J Bridge Eng 2021;26(3):05020013.
[48] Zhou LR, Liang CF, Chen L, Xia Y. Numerical simulation method of thermal analysis for bridges without using field measurements. In: Proceedings of the sixth international workshop on performance, protection and strengthening of structures under extreme loading (PROTECT). CHN: Guangzhou; 2017.
[49] Carboni B, Lacarbonara W. A three-dimensional continuum approach to the thermoselasto- dynamics of large-scale structures. Eng Struct 2012;40:155–67.
[50] Ali MA, Shimoda M. On multiphysics concurrent multiscale topology optimization for designing porous heat-activated compliant mechanism under convection for additive manufacture. Eng Struct 2023;294:116756.